A Regionally Robust High-Spatial-Resolution Aerosol Retrieval Algorithm for MODIS Images Over Eastern China

Jing Wei, *Student Member, IEEE*, Zhanqing Li, Yiran Peng, Lin Sun, and Xing Yan

Abstract—Moderate resolution imaging spectroradiometer (MODIS) has been widely used in related aerosol studies because of its long data records. However, operational aerosol optical depth (AOD) products at coarse spatial resolutions limit their applications on small and medium scales. Thus, high-spatial-resolution AOD products are needed. In this paper, a regionally robust high-resolution aerosol retrieval algorithm is developed for MODIS images over Eastern China which has complex surfaces and severe air pollution. Several major challenges in aerosol retrieval are resolved including: 1) surface reflectance by correcting for the effects of surface bidirectional reflectance distribution function using the RossThick-LiSparse model; 2) aerosol models assumed by time-series data analysis with historical aerosol optical properties measurements from the Aerosol Robotic Network (AERONET) sites; and 3) cloud screening using the proposed universal dynamic threshold cloud detection algorithm. Moreover, gas (i.e., ozone and water vapor) absorption is also corrected. Finally, our AOD retrievals are compared with the newest AERONET Version 3 Level 2.0 AOD ground-based measurements, latest MODIS Collection 6.1 AOD products at 3- and 10-km resolutions, and multiangle implementation of the atmospheric correction (MAIAC) AOD product at a 1-km resolution. The results suggest that our algorithm performs well over dark vegetated and bright urban surfaces and that 78.56% of the retrievals meet the acceptable expected error of $\pm(0.05\% + 20\%)$ with a mean absolute error and a root-mean-square error of 0.074 and 0.125, respectively. Comparison results indicate that the newly generated 1-km AOD data set is much better than the routine MOD04 3- and 10-km dark target data sets, and slightly better than the 10-km deep blue (with lower resolution) and 1-km MAIAC (with narrower space coverage) AOD products.

This attests to the robustness of our algorithm that generates an AOD product with a more continuous coverage and finer resolution over complex surfaces.

Index Terms—1-km resolution, aerosol optical depth (AOD), Aerosol Robotic Network (AERONET), MOD04, moderate resolution imaging spectroradiometer (MODIS), multiangle implementation of the atmospheric correction (MAIAC).

I. INTRODUCTION

ATMOSPHERIC aerosols are liquid or solid suspended particles with aerodynamic diameters ranging from 10^{-3} to $10^2 \mu$m. They can be condensate nodules of water droplets and ice crystals, absorbers, and scatterers of solar radiation, and are involved in chemical cycles. Therefore, aerosols have direct and indirect effects on the ecological environment [1]–[4] and climate [5]–[7] due to aerosol–radiation interactions, aerosol–cloud interactions [8]–[10], and human health [1], [5]. A better understanding of the impacts requires a good knowledge of aerosol amount and characteristics. Satellite remote sensing provides an effective way to obtain the spatial distributions and temporal variations of aerosols on long time and large spatial scales.

The spectral aerosol optical depth (AOD) is a key measure of aerosol loading that is defined as the total extinction due to the scattering and absorption of solar light by aerosol particles along an atmospheric path [11]. Space-borne passive imaging radiometers can retrieve AOD based on an atmospheric radiative transfer model [12], [13]. The basic principle underlying such a model is to separate the contributions of the atmosphere and the earth's surface from the satellite-received signal. While satellite remote sensing has many merits over ground measurements, the former is subject to more challenges and uncertainties due to the radiometric calibration, cloud screening, surface reflection, and aerosol model assumption [13].

It is especially challenging to retrieve AOD over land because land has complex surfaces and aerosol compositions that vary with time and location. In the visible wavelengths, both AOD and surface reflection contribute to the satellite signal. To differentiate them, Kaufman *et al.* [14] proposed to use the ratio of surface reflectances in the visible and short-wave infrared (SWIR) channels (e.g., 2.1 μm) because of their nearly constant ratios. Note that aerosols have negligible scattering in the SWIR region, allowing for the determination of surface reflectance. This is the foundation of the so-called dark

target (DT) algorithm [14]–[16]. However, it is not applicable to bright surfaces such as deserts. Therefore, a deep blue (DB) algorithm was developed based on the fact that bright surfaces are much darker at shorter wavelengths [17]–[19].

The moderate resolution imaging spectroradiometer (MODIS) sensor was successfully launched onboard the Terra satellite in December 1999 and has provided daily global aerosol products at spatial resolutions of 3 km (MOD04_3K) and 10 km (MOD04_L2). These aerosol products include retrievals from the DT algorithm over land and ocean, the DB algorithm over land only, and a combined DT and DB (DTB) algorithm over land and ocean [16]. However, despite good local or global accuracies [16], [20], [21], these products are limited in exploring the spatial distributions and variations in atmospheric pollutants at small to medium scales because of their coarse spatial resolutions.

Therefore, an increasing number of studies have focused on aerosol retrievals at high spatial resolutions in recent years. For example, Wong *et al.* [22] developed a new aerosol retrieval algorithm based on MODIS apparent reflectance images and using the minimum reflectance technique. AODs at a 500-m resolution were subsequently retrieved over Hong Kong and the Pearl River Delta. Lyapustin *et al.* [23] presented a multi-angle implementation of the atmospheric correction (MAIAC) algorithm with time-series image-based processing and generated reasonably accurate aerosol retrievals using MODIS images at a 1-km resolution. Bilal *et al.* [24] proposed a simplified aerosol retrieval algorithm with empirical parameters involving local Aerosol Robotic Network (AERONET) ground-based AOD measurements. This algorithm was used to retrieve AODs at a 500-m resolution over Hong Kong based on MODIS images from the green channel. Wei and Sun [25] proposed a high-spatial-resolution aerosol retrieval algorithm with a prior surface reflectance database support for MODIS images at a 1-km resolution over bright urban areas, and then improved and validated it at the global scale over land [26].

The objective of this paper is to develop a regionally robust aerosol retrieval algorithm that can generate AODs at a 1-km spatial resolution from MODIS images for application to aerosol studies focused on small- and medium-scale areas. The following challenges are considered and addressed:
1) surface reflectance estimated from the RossThick-LiSparse model to minimize the effects of the surface bidirectional reflectance distribution function (BRDF);
2) aerosol type determined by a long-time-series analysis of optical properties from historical local ground-based measurements;
3) cloud screening using the Universal Dynamic Threshold Cloud Detection Algorithm (UDTCDA) [27];
4) gas absorption corrected with more accurate approximations.

A regional high-resolution aerosol retrieval algorithm is developed based on these considerations. MOD02 L1B images at a 1-km resolution from 2010 to 2014 over Eastern China are collected for the study. This part of China has complex surface structures and experiences severe air pollution. Meanwhile, AERONET AOD ground measurements and MODIS AOD

products are also collected for validation and comparison purposes.

II. DATA SOURCES

A. AERONET Aerosol Measurements

The AERONET provides a long-term and freely available database of aerosol optical properties and their inversion products from sites around the world. Spectral AODs covering the visible (0.34 μm) to NIR (1.02 μm) wavelengths are reported every 15 minutes with a low uncertainty of ~0.01–0.02. AOD measurements are available at three data quality levels (L): L1.0 (unscreened), L1.5 (cloud-screened), and L2.0 (cloud-screened and quality-assured). Version (V) 3 L2.0 AERONET data were released in January 2018 [28]–[30], making available AOD data at near real time with enhanced cloud screening and quality assurance (QA). V3 L2.0 aerosol optical properties at the Beijing (39.98°N, 116.38°E), Beijing_RADI (40.01°N, 116.38°E), Beijing_CAMS (39.93°N, 116.32°E), Xianghe (39.75°N, 116.96°E), and Xinglong (40.40°N, 117.58°E) sites during 2010–2014 are selected for this paper as the ground truth.

B. MODIS Operational Aerosol Products

MODIS Collection 6.1 (C6.1) aerosol products have recently been released with continuous efforts and improvements to both data radiometric calibration and aerosol retrieval algorithms. Therefore, the latest MOD04 C6.1 3-km DT, and 10-km DT, DB, and DTB AOD retrievals are used here. Only those recommended high-quality aerosol retrievals passing the QA are used for comparison purposes (QA = 3 for DT and DTB, and QA $\geq$ 2 for DB) [30].

MAIAC AOD product at 1-km resolution is also obtained for comparison purposes. This product is generated based on the semianalytical Green's function solution for the apparent reflectance combined with a linear BRDF model. It assumes a Lambertian equivalent reflector and eight customized regional aerosol models defined based on AERONET climatology. The lookup table (LUT) approach is used to retrieve AOD. For this paper, only retrievals passing the cloud screening (QA$_{CloudMask}$ = Clear) and adjacency (QA$_{AdjacencyMask}$ = Clear) tests are used here [31]. Table I lists the data sets used in this paper.

III. METHODOLOGY

Here, a regionally robust aerosol retrieval algorithm at a high resolution of 1 km is developed for MODIS images based on the LUT approach, precalculated using the vector radiation transfer model [32], [33]. Inputs to the algorithm include the total gas [i.e., ozone (O_3), water vapor (H_2O)] amount, top-of-the-atmosphere (TOA) reflectances calculated from MOD02 L1B radiance images, surface reflectance, and aerosol optical properties. Based on the atmospheric radiative transfer model, the satellite-received TOA reflectance is a function of atmospheric path reflectance including molecular

TABLE I
SUMMARY OF DATA SETS USED IN THIS PAPER

Dataset	Scientific Data Set	Contents	Resolutions
MOD021KM	EV_500_Aggr1km_RefSB	Calibrated radiance	Daily, 1 km
		Height	Daily, 1 km
MOD04_3K	Optical_Depth_Land_And_Ocean	DT AOD (QA=3)	Daily, 3 km
MOD04_10K	Optical_Depth_Land_And_Ocean	DT AOD (QA=3)	Daily, 10 km
	Deep_Blue_Aerosol_Optical_Depth_550_Land_Best_Estimate	DB AOD (QA≥2)	Daily, 10 km
	AOD_550_Dark_Target_Deep_Blue_Combined	DTB AOD (QA=3)	Daily, 10 km
MAIAC	Optical_depth_055	AOD	Daily, 1 km
MCD43A4	MODIS BRDF/Albedo Product	Nadir BRDF-Adjusted reflectance	Daily, 500 m
AERONET	Version 3 Level 2.0	Optical properties	15 min/ monthly, -

(Rayleigh) and aerosol scattering, and the surface function:

$$\rho^* = T_{og}T_{O_3}\left[(\rho_{\mathrm{Aer}} - \rho_{\mathrm{Ray}(P_0)})T_{H_2O}\left(\frac{C_{H_2O}}{2}\right) + \rho_{\mathrm{Ray}(P)} \right.$$
$$\left. + T_{H_2O}(C_{H_2O})T_{\theta_s}T_{\theta_v}\frac{\rho_s}{1 - \rho_s S_\lambda}\right] \quad (1)$$

where ρ^* is the TOA reflectance; ρ_{Aer} is the atmospheric intrinsic reflectance; $\rho_{\mathrm{Ray}(P)}$ is the Rayleigh intrinsic reflectance at actual pressure (P, unit: atm); P_0 is the standard pressure; T_{H_2O}, T_{O_3}, and T_{og} are the downward and upward gaseous transmissions for the total O_3, H_2O, and other gases, respectively; C_{H_2O} is the total column amount of H_2O; θ_s is the solar zenith angle and θ_v is the viewing zenith angle; T_{θ_s} and T_{θ_v} represent the total downward and upward atmospheric transmissions; S is the atmospheric spherical albedo; and ρ_s is the surface reflectance.

The channel-dependent parameters including ρ_{Aer}, T_{θ_s}, T_{θ_v}, and S are calculated with the Second Simulation of the Satellite Signal in the Solar Spectrum (6S) V2.1 radiative transfer model for different geometries, AODs, and aerosol-type models, and stored in preconstructed LUTs. Rayleigh scattering has significant impacts on the visible channels (especially the blue channel) and can be corrected with the Rayleigh phase function and Rayleigh optical depth. The Rayleigh optical depth is calculated by scaling the Rayleigh optical depth at standard pressure by the ratio of the actual pressure to the standard pressure [34]. The approaches used to estimate other parameters (T_{H_2O}, T_{O_3}, T_{og}, ρ_s) and optical properties for different aerosol types are introduced next.

A. Gas Absorption Correction

Satellite data are measured at the wavelengths where the gas absorption is small but not zero in these window channels. In the solar spectrum, gaseous absorption is principally due to oxygen (O_2), O_3, water vapor (H_2O), carbon dioxide (CO_2), methane (CH_4), and nitrous oxide (N_2O). O_2, CO_2, CH_4, and N_2O are assumed constant and uniformly mixed in the atmosphere. However, H_2O and O_3 concentrations are always changing depending on time and location, and are the most important gases to consider, especially in the visible channels. Gas absorption (except for H_2O) is assumed to occur above the scattering layers of the atmosphere. H_2O absorption is negligible at short wavelengths where Rayleigh scattering is significant, and Rayleigh reflectance is not attenuated. Also, aerosols are assumed to be well mixed with H_2O, and the aerosol path reflectance is affected by half of the total column amount of H_2O on average. The gas transmissions for H_2O, O_3, and other gases at a given wavelength (λ) can be approximated by the following [35]:

$$T_{O_3}^\lambda = \exp\left[-\left(M\tau_{O_3}^\lambda\right)\right] = \exp\left[-\left(a_0^\lambda + a_1^\lambda MC_{O_3}\right)\right] \quad (2)$$

$$T_{H_2O}^\lambda = \exp\left[-\left(M\tau_{H_2O}^\lambda\right)\right] = \exp\left\{-\exp\left[b_0^\lambda + b_1^\lambda\right.\right.$$
$$\left.\left. \times \ln(MC_{H_2O}) + b_2^\lambda \ln(MC_{H_2O})^2\right]\right\} \quad (3)$$

$$T_{og}^\lambda = \exp\left[-\left(M\tau_{og}^\lambda\right)\right] \quad (4)$$

$$M = M(\theta_s) + M(\theta_v) = \frac{1}{\cos\theta_s + c_{i,1}\theta_s^{c_{i,2}}(c_{i,3} - \theta_s)^{c_{i,4}}}$$
$$+ \frac{1}{\cos\theta_v + c_{i,1}\theta_v^{c_{i,2}}(c_{i,3} - \theta_v)^{c_{i,4}}} \quad (5)$$

where M is the air mass factor accounting for climatological differences of vertical profiles of each gas constituent, and $c_{i,1}$, $c_{i,2}$, $c_{i,3}$, and $c_{i,4}$ (i is the gas type) represent the air mass factor coefficients and are given in [36]. Coefficients a_0^λ, a_1^λ and b_0^λ, b_1^λ, b_2^λ are the H_2O and O_3 absorption coefficients at different wavelengths [35], and C_{O_3} and C_{H_2O} are the total amounts of O_3 (in Dobson units) and H_2O (in cm) along an atmospheric path, obtained from the ERA-interim daily measurements [37]. The optical depths $\tau_{O_3}^\lambda$, $\tau_{H_2O}^\lambda$, and τ_{og}^λ represent the optical depths of O_3, H_2O, and other gases. If O_3 and H_2O measurements are missing, empirical optical depths are used [35].

B. Surface Reflectance Estimation

Surface reflectance is one of the key parameters for aerosol retrievals over land due to complex surface types and structures. Our previous studies have revealed that a 1% estimation error in the surface reflectance can lead to a ~10% AOD retrieval error for dark surfaces and that the retrieval error can increase with increasing surface reflectance [20]. Recently, aerosol retrievals have been done using precalculated surface reflectance databases that depend on the TOA reflectance or atmospheric-corrected surface reflectance products and that use the minimum value synthesis method to minimize the effects of aerosols and clouds. These retrievals have high accuracies [17], [25], [26], [38]. However, there may be inevitable over- or under-estimations of surface reflectances over varying underlying surfaces and the effects of surface bidirectional reflectance distributions were not considered in these retrieval algorithms. With this in mind, daily surface reflectance images for three visible channels are calculated using the BRDF parameters provided by the MCD43 product with the RossThick-LiSparse model to provide the actual

surface reflectance and to minimize the effects of surface BRDF in this paper.

The land surface BRDF reflectance can be calculated from a linear kernel-driven model, which is the sum of three theoretically constructed kernels representing basic scattering types including the isotropic, volumetric, and geometric-optical types [39]:

$$\rho^R(\theta_s, \theta_v, \varphi) = f_{\text{iso}} + f_{\text{vol}} K_{\text{RT}}(\theta_s, \theta_v, \varphi) + f_{\text{geo}} K_{\text{LS}}(\theta_s, \theta_v, \varphi) \tag{6}$$

where ρ^R is the surface bidirectional reflectance, φ is the relative azimuth angle, and f_{iso}, f_{vol}, and f_{geo} are the coefficients of the three kernels representing the weights of isotropic scattering, volume scattering, and surface scattering, respectively. They are available from the MCD43 BRDF/Albedo model parameters product. K_{RT} and K_{LS} are the RossThick (7) [40], [41] kernel and the LiSparse (9) [42], [43] kernel, respectively,

$$K_{\text{RT}}(\theta_s, \theta_v, \varphi) = \left[\left(\frac{\pi}{2} - \delta\right)\cos\delta + \sin\delta\right]/[\cos\theta_s$$
$$+ \cos\theta_v] - \frac{\pi}{4} \tag{7}$$

$$\delta = \arccos(\cos\theta_s\cos\theta_v + \sin\theta_s\sin\theta_v\cos\varphi) \tag{8}$$

$$K_{\text{LS}}(\theta_s, \theta_v, \varphi) = O(\theta_s, \theta_v, \varphi) - \sec\theta_s - \sec\theta_v$$
$$+ \frac{1}{2}(1 + \cos\delta)\sec\theta_s\sec\theta_v \tag{9}$$

$$O(\theta_s, \theta_v, \varphi) = (1/\pi)(t - \sin t\cos t)(\sec\theta_s + \sec\theta_v) \tag{10}$$

$$\cos t = 2\sqrt{D^2 + (\tan\theta_s\tan\theta_v\sin\varphi)^2}/(\sec\theta_s + \sec\theta_v) \tag{11}$$

$$D = \sqrt{\tan^2\theta_s + \tan^2\theta_v - 2\tan\theta_s\tan\theta_v\cos\varphi} \tag{12}$$

where δ is the phase angle and O is the overlap area between the view and solar shadows. The $\cos t$ term is constrained to the range [1, 1] because values outside of this range imply no overlap and should be disregarded.

C. Aerosol-Type Assumption

Aerosol types mainly characterize the physical and chemical properties of aerosols in a certain region, and different aerosols vary greatly in the source, scale, concentration, composition, and spectral distribution with time and space in the atmosphere over land. The optical properties of aerosols are also different. Aerosol type is another key factor to consider when improving the retrieval accuracy. The optical properties describing the aerosol type mainly include the single scattering albedo (ω), the asymmetry factor (g), and the complex part of the refractive index (CRI). The ω is the sum extinction caused by scattering and represents the ability to absorb and scatter electromagnetic radiation. The g is the relative dominance of forward and backward scattering and remains unchanged for an aerosol type. The CRI indicates the ability of particles to scatter and absorb light. The real part (RP) of the CRI describes the ability of aerosol particles to attenuate radiative energy, and the imaginary part of the CRI describes the ability of aerosol particles to absorb radiative energy.

For this, AERONET V3 monthly measurements of the main aerosol optical properties from five sites in Eastern China
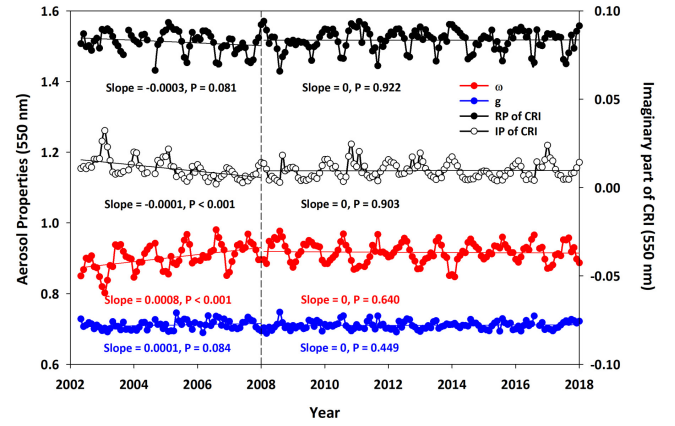

Fig. 1. Long-term monthly variations of aerosol properties (550 nm) over Eastern China during the period 2002–2017.

from 2002 to 2017 are examined. Fig. 1 shows the long-term temporal variations of above four optical properties at 550 nm interpolated with the Ångström Exponent algorithm over Eastern China. Two distinct trends are seen, roughly before and after the year 2008. Before 2008, ω has an increasing trend of 0.08% yr^{-1} ($P < 0.001$), suggesting that aerosols were gradually becoming less absorbing during this period. Similarly, g shows a relatively smaller increasing trend of 0.01% yr^{-1} ($P < 0.1$). However, the RP and IR of the CRI show decreasing trends of 0.03% yr^{-1} ($P < 0.1$) and 0.01% yr^{-1} ($P < 0.001$), respectively. By contrast, during 2008–2017, all the four optical properties are much more stable with slopes close to 0, but there are seasonal variations in four properties. Maximum and minimum values of ω are found in summer and winter, respectively. The g varies in a similar way but with a smaller magnitude. However, the RP and IR of the CRI have opposite seasonal variations with maximum and minimum values found in winter and summer, respectively. In general, despite clear seasonal differences, the four optical properties change little during a particular season. Therefore, we assume that the dominant aerosol type is a function of season. Four customized seasonal aerosol types are defined and used for aerosol retrievals over Eastern China in this paper. The four optical properties are seasonally averaged based on monthly measurements from 2008 to 2017. Table II lists the wavelength-dependent optical properties of the assumed seasonal aerosol models used to retrieve AODs in this paper.

D. Pixel Selection

Before doing the aerosol retrieval, all unsuitable pixels must be filtered out and masked, including pixels containing clouds, snow/ice, and water. For this purpose, our proposed UDTCDA with the prior support of a precalculated surface reflectance database [27] for MODIS images is selected to detect and mask potential clouds (13)–(16). Moreover, a ratio involving TOA 0.86- and 1.24-μm reflectances and 11-μm brightness temperatures (BT$_{31}$) is used to identify and mask potential snow and ice (17). Last, water bodies are determined by the normalized difference vegetation index (NDVI) if it is less

TABLE II

OPTICAL PROPERTIES OF FOUR CUSTOMIZED SEASONAL AEROSOL MODELS USED IN THE AOD RETRIEVAL

Model	ω (0.47/0.55/0.66 μm)	g (0.47/0.55/0.66 μm)	RP-CRI (0.47/0.55/0.66 μm)	IP-CRI (0.47/0.55/0.66 μm)	Fine model (C/R/S)	Coarse model (C/R/S)
Spring	0.920/0.925/0.932	0.710/0.684/0.662	1.521/1.529/1.536	0.008/0.007/0.006	0.151/0.217/0.528	0.129/2.721/0.581
Summer	0.947/0.948/0.949	0.720/0.693/0.669	1.478/1.479/1.480	0.007/0.006/0.006	0.264/0.254/0.532	0.190/2.578/0.565
Autumn	0.910/0.912/0.913	0.709/0.683/0.660	1.520/1.522/1.524	0.013/0.011/0.011	0.068/0.174/0.472	0.088/2.262/0.653
Winter	0.889/0.893/0.896	0.704/0.677/0.654	1.533/1.539/1.545	0.016/0.014/0.013	0.076/0.189/0.501	0.074/2.913/0.615

*Note: ω, g, RP-CPI, and IP-CPI stand for the single scattering albedo, the asymmetry factor, and the real and imaginary parts of the refractive index; C, R, and S represent the volume concentration (μm³/μm²), mean radius (μm), and standard deviation for the size distribution parameters, respectively.

TABLE III

PARAMETER SETTING IN THE LUT CONSTRUCTION

Parameter	Values
AOD	[0, 0.01, 0.05, 0.1, 0.2, 0.3, …, 1.0, 1.2, 1.5, 2.0, 2.5, 3.0]
Surface reflectance	[0, 0.01, 0.02, 0.03, …, 0.2]
Solar zenith angle (°)	[0, 6, 12, 18, …, 78]
Satellite zenith angle (°)	[0, 6, 12, 18, …, 78]
Relative azimuth angle (°)	[0, 10, 20, 30, …, 180]

than 0.1:

$$\rho_B^{*'} = 0.793 \times \rho_B + 0.004 \times \cos\theta_s \cos\theta_v + 0.158 \quad (13)$$

$$\rho_G^{*'} = 0.807 \times \rho_G + 0.025 \times \cos\theta_s \cos\theta_v + 0.125 \quad (14)$$

$$\rho_R^{*'} = 0.843 \times \rho_R + 0.017 \times \cos\theta_s \cos\theta_v + 0.112 \quad (15)$$

$$C_i = \rho_i^* - \rho_i^{*'} > 0, \quad \text{and Final} = C_B \cup C_G \cup C_R \quad (16)$$

$$\text{TOA}_{\text{ratio}} = \frac{\rho_{0.86}^* - \rho_{1.24}^*}{\rho_{0.86}^* + \rho_{1.24}^*} > 0.1 \quad \text{and } BT_{31} < 285 \text{ K} \quad (17)$$

where $\rho_i^{*'}$ represents the simulated TOA reflectances of the blue (B), green (G), and red (R) channels; ρ_i and ρ_i^* represent the surface reflectance and TOA reflectance, respectively; C_i represents the cloud mask for different channels, and Final represents the final cloud mask.

E. Aerosol Retrieval

In this paper, the LUT approach is used to retrieve AOD. The LUTs for four seasonal aerosol models are constructed under different atmospheric, surface, and geometric conditions for the blue and red channels using the 6S model (Table III). A pixel passing all the above tests is selected for the aerosol retrieval through the pixel-by-pixel look-up approach. To minimize the effects of the signal-to-noise ratio, a spatial homogeneity filter with a 3 × 3 running average window is applied to the final retrievals. The aerosol retrieval procedure is implemented by a C++ program, and takes only about 2 minutes to generate an image at 1-km resolution. Fig. 2 shows the flowchart of the regionally robust aerosol retrieval algorithm proposed here.
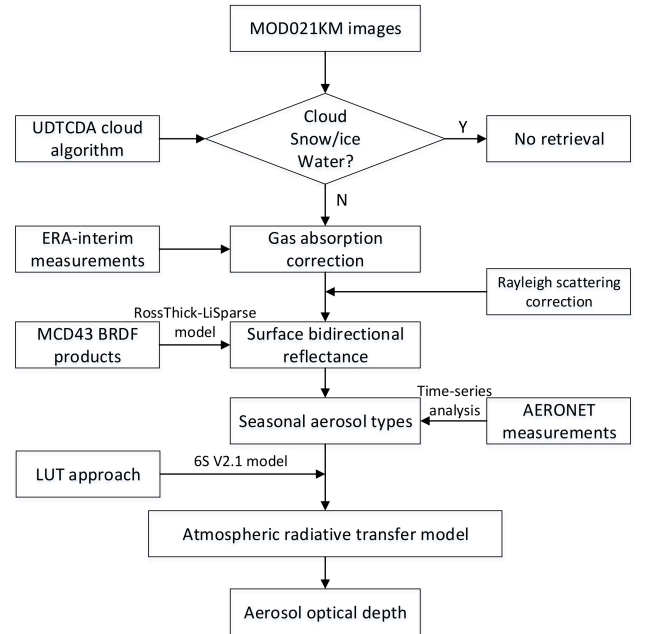

Fig. 2. Flowchart of the regionally robust aerosol retrieval algorithm.

IV. EVALUATION APPROACHES

MODIS Level 1B radiance images at a spatial resolution of 1 km (MOD021KM) from 2010 to 2014 over Eastern China are collected to do AOD retrievals. The new 1-km AOD retrievals are first validated against AERONET V3 L2.0 AOD measurements at five sites. MOD04 C6.1 DT 3-km, DT 10-km, DB 10-km, and DTB 10-km retrievals, and MAIAC 1-km retrievals for the same period are also used for comparison purposes. In addition, the spatial distributions of all these aerosol products are compared. All MODIS-based AOD retrievals within a sampling window of 5 × 5 pixels around an AERONET site are first averaged to obtain a mean value for the AOD retrieval. A minimum of two AERONET AOD measurements at each site within ±30 min of the MODIS Terra overpass time are averaged to obtain a temporally matched ground-based retrieval to use as the ground truth [20]. Note that the AERONET does not provide AOD retrievals at 550 nm. Therefore, 550-nm AODs are generated through interpolation using the Ångström Exponent algorithm [20], [39]. The slope and intercept of a linear regression equation, the correlation coefficient (R), and four evaluation metrics, i.e., the mean absolute error (MAE), the root-mean-square

TABLE IV
VALIDATION OF AOD RETRIEVALS AT EACH SITE OVER EASTERN CHINA FROM 2010 TO 2014

Site	N	R	MAE	RMSE	RMB	Within EE (%)	Above EE (%)	Below EE (%)
Beijing	452	0.918	0.085	0.146	1.032	74.56	14.38	11.06
Beijing_CAMS	131	0.955	0.080	0.132	1.124	78.63	18.32	03.05
Beijing_RADI	87	0.892	0.076	0.120	1.013	74.72	13.79	11.49
Xianghe	455	0.932	0.080	0.128	1.061	76.04	17.14	06.82
Xinglong	330	0.932	0.050	0.082	0.977	88.48	06.67	04.85
All sites	1455	0.929	0.074	0.125	1.042	78.56	13.81	07.63

error (RMSE), the relative mean bias (RMB), and MODIS expected errors (EE, $\pm[0.05\% + 20\%]$) for DB AOD retrievals over land are selected to evaluate accuracies and uncertainties.

V. RESULTS AND DISCUSSION

A. Validation Against AERONET Ground Measurements

Our 1-km MODIS AOD retrievals are first validated against AERONET AOD measurements from 2010–2014 at each site in Eastern China (Table IV). Beijing, Beijing_CAMS, and Beijing_RADI are three typical urban sites located in the center of Beijing City, while Xianghe and Xinglong are in the suburbs close to croplands. The 452 matched retrievals from our algorithm at the Beijing site are highly correlated with AERONET AOD measurements ($R = 0.918$). About 74% of them fall within the EE envelope with average MAE and RMSE values of 0.085 and 0.146, respectively. Due to shorter records, a smaller number of matched retrievals from our algorithm are generated at the Beijing_CAMS and Beijing_RADI sites, i.e., 131 and 87, respectively. These retrievals agree well with AERONET AOD measurements ($R = 0.955$ and 0.892), and 78.63% and 74.71% of them fall within their respective EE envelopes with MAEs of 0.080 and 0.076, and RMSEs of 0.132 and 0.120, respectively. This suggests that the new algorithm works well for bright urban areas. Moreover, at the two vegetated sites, 455 and 330 matched retrievals from our algorithm agree well with surface measurements ($R = 0.933$ and 0.932). The percentage of retrievals falling within the EE envelope are 76.04% and 88.48% with average MAE values of 0.080 and 0.049, and RMSE values of 0.128 and 0.082. These results also suggest that the new algorithm works well for vegetated areas. On a regional scale, a total of 1455 matched retrievals from our algorithm from five sites in the study area from 2010 to 2014 were collected. Our AOD retrievals agreed well with AERONET AOD measurements ($R = 0.929$). In general, 78.56% of them fell within the EE envelope with an average MAE of 0.074 and RMSE of 0.125. The overall good quality of the AOD retrievals demonstrates that this newly developed algorithm can be applied to data collected over both bright and dark surfaces.

B. Comparison With Operational MOD04 AOD Products

Figs. 3 and 4 show comparisons between our new 1-km AOD retrievals and operational MOD04 3- and 10-km AOD retrievals against AERONET AODs over Eastern China from
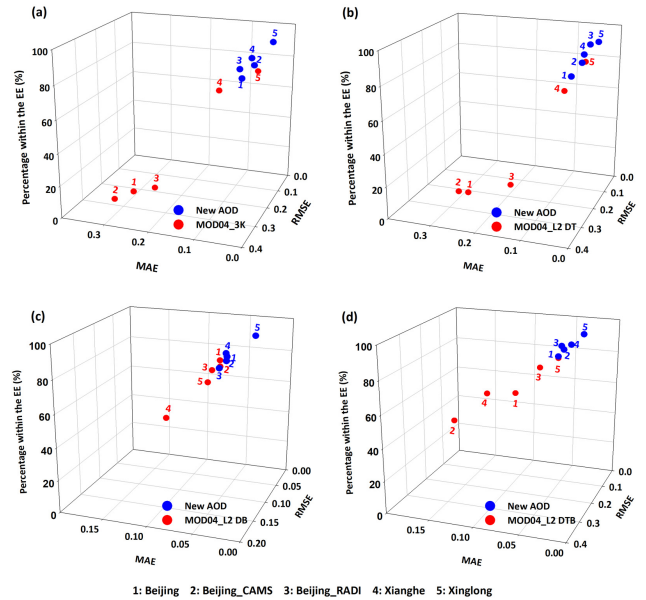

Fig. 3. 3-D scatterplots of our 1-km AOD retrievals matched with MOD04. (a) 3-km DT, (b) 10-km DT, (c) DB, and (d) DTB AOD retrievals at each site in Eastern China from 2010 to 2014. AERONET V3 L2.0 AOD measurements are used as the ground truth. Sites 1–3 are urban sites, and sites 4–5 are suburban sites close to croplands.

2010 to 2014. MOD04_3K DT AODs agree well with AERONET AOD measurements at the two vegetated sites with more than 72% of the data samples falling within the EE envelopes and with small MAE and RMSE values [Fig. 3(a)]. However, less agreement is found at three urban sites with fewer retrievals falling within EE envelopes, and with larger mean MAE and RMSE values. By contrast, AOD retrievals from our algorithm agree well with AERONET AODs at all sites as shown by the cluster of blue points in the upper right corner of Fig. 3(a). On a regional scale, there are 475 matched retrievals collected from the five sites. The MOD04 3-km DT product does not perform well with less than half of the retrievals falling within the EE envelope and with an average MAE of 0.164 and RMSE of 0.224 [Fig. 4(a)]. A large overestimation of the aerosol loading is seen with more than 45% of the matched retrievals falling above the EE envelope. Our 1-km AOD product performs better with ~80.84% of the matched retrievals falling within the EE envelope, and with lower MAE and RMSE values (0.074 and 0.125, respectively).
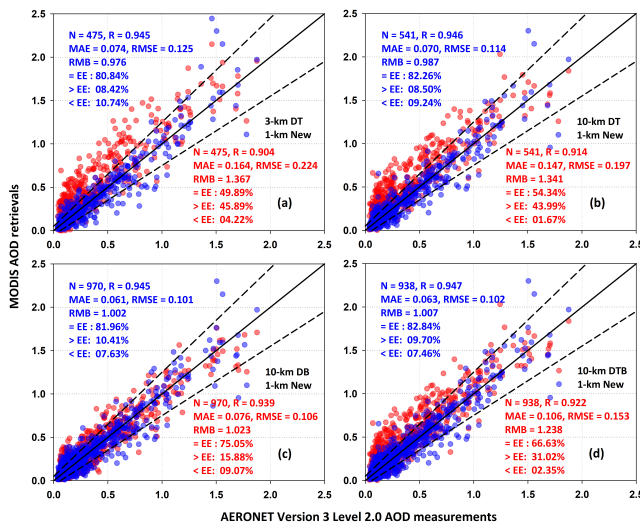
Fig. 4. Scatterplots of our 1-km AOD retrievals matched with MOD04. (a) 3-km DT, (b) 10-km DT, (c) DB, and (d) DTB AOD retrievals as a function of AERONET V3 L2.0 AOD measurements at each site in Eastern China from 2010 to 2014. The blue and red dots represent our new and MOD04 retrievals, respectively. The dotted lines represent EE lines and the solid black lines represent the 1:1 line.

The performance of the MOD04 10-km DT AOD product is similar to that of the MOD04 3-km DT AOD product because they are generated using the similar DT algorithm [Fig. 3(b)]. Our algorithm performs better at all sites as shown by the higher fraction of retrievals falling within the EE envelope and smaller MAE and RMSE values. On a regional scale, 541 matched retrievals are collected. The 10-km DT retrievals do not perform well with 54% of the matchups falling within the EE envelope and with an average MAE of 0.147 and RMSE of 0.197 [Fig. 4(b)]. Note that there are still noticeable overestimations with 44% of the matched retrievals falling above the EE envelope. The site-scale validation results show that 85% (86%), 86% (82%), and 73% (78%) of the MOD04 3-km (10-km) DT matched retrievals fall above the EE envelopes at Beijing, Beijing_CAMS and Beijing_RADI sites, respectively. By contrast, only ~10%–26% of the matched retrievals are overestimated at the two vegetated sites. This suggests that most of the overestimations occur at the urban sites. The main reason is that the DT algorithm seriously underestimates the surface reflectance and is not suitable for retrieving AODs over bright urban surfaces [26]. These results illustrate that although the surface modeling has been improved in the latest C6.1 DT algorithm, its limitation still exists to large degree. Our 1-km AOD retrievals are better correlated with AERONET AODs than are the MOD04 10-km DT AOD retrievals, and a higher fraction of the matchups (~82%) fall within the EE envelope. The average MAE and RMSE values are reduced by 110% and 73%, respectively.

The DB algorithm can generate AOD retrievals over bright surfaces. Noticeable improvements in all metrics for the DB retrievals at the urban sites are thus seen [Fig. 3(c)]. However, the DB retrievals are slightly less reliable than the DT retrievals at the two vegetated sites. Our algorithm performs as well as the DB algorithm at the three urban sites and better at the vegetated sites. On a regional scale, the DB algorithm can

provide about 1.8 times more retrievals than the DT algorithm [Fig. 4(c)]. The DB retrievals agree well with AERONET AOD measurements ($R = 0.939$) with 75% of the retrievals falling within the EE envelope, and with an average MAE of 0.077 and RMSE of 0.106. These results show that the DB algorithm performs better than the DT algorithm due to its more accurate approach in estimating the surface reflectances of bright surfaces. In general, our AOD retrievals are in better agreement with the AERONET AOD measurements than are the DB retrievals and are slightly better than the DB retrievals themselves.

The performance of the DTB algorithm at different sites is mixed [Fig. 3(d)]. In general, compared to DT products, the metrics are improved. However, compared to the DB product, retrievals at the urban sites are less accurate. DTB retrievals are less reliable than DT retrievals at the vegetated sites but overall better than the DB retrievals at the vegetated sites. Our retrievals are generally better than the DTB retrievals with improved metrics at all sites, especially at the urban sites. On a regional scale, there are 938 matched retrievals. DTB retrievals correlate well with AERONET AOD measurements with ~66% of them falling within the EE envelope, and with MAE and RMSE values of 0.106 and 0.153, respectively. However, ~34% of the DTB AOD retrievals fall above the EE envelope [Fig. 4(d)]. In general, DTB retrievals are much better than DT retrievals but less reliable than DB retrievals. The AOD retrievals from our algorithm are still more correlated with AERONET AOD measurements ($R = 0.957$). Compared with the DTB retrievals, a higher fraction of retrievals from our algorithm fall within the EE envelope (~83%) and have lower MAE and RMSE values (0.063 and 0.102, respectively). These results suggest that the new algorithm performs better overall than the algorithms that generate MOD04 AOD products over both bright and dark surfaces, mainly because of regional improvements in surface reflectance estimations and aerosol model assumptions.

C. Comparison With High-Resolution MODIS AOD Products

Fig. 5 shows our 1-km AOD retrievals and MAIAC 1-km AOD retrievals matched with AERONET AOD measurements at the five sites in Eastern China from 2010 to 2014. The MAIAC retrievals agree well with AERONET AODs at both urban and vegetated sites with more than 75% of the matched retrievals falling within the EE envelope and with MAE and RMSE values less than 0.07 and 0.1, respectively. Our 1-km AOD retrievals are within ±0.012, ±0.004, and ±5% of the MAIAC AOD retrievals in terms of MAE, RMSE, and the fraction of retrievals falling within the EE envelope, respectively, at all sites.

On a regional scale, there are 670 matchups. MAIAC AODs agree well with AERONET AODs ($R = 0.941$) with 82% of the retrievals falling within the EE envelope, and with small MAE and RMSE values of 0.061 and 0.091, respectively. Most of our AOD retrievals overlap with the MAIAC AOD retrievals. In general, our AOD retrievals are more correlated with ground measurements ($R = 0.942$) and have a larger fraction of retrievals falling within the EE envelope (~84%). The MAE and RMSE values are smaller than
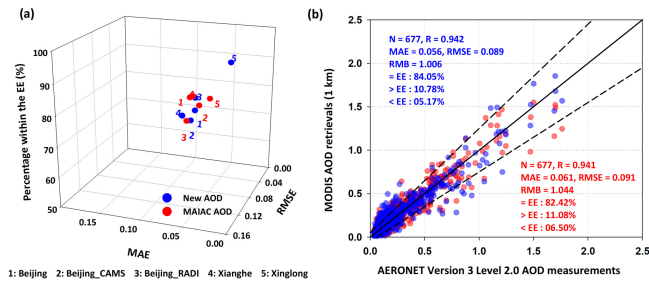
Fig. 5. (a) 3-D scatterplots of our 1-km AOD retrievals matched with MAIAC 1-km AODs at each site. (b) Scatterplots of all matched retrievals as a function of AERONET V3 L2.0 AOD measurements from 2010 to 2014. The blue and red dots represent our new and MAIAC AOD retrievals, respectively. The dotted lines represent EE lines and the solid black line represents the 1:1 line.

those of the MAIAC retrievals (0.056 and 0.089, respectively). These results illustrate that our algorithm performs slightly better than the MAIAC algorithm in areas with complex surfaces.

Furthermore, compared with the same 1-km AOD retrievals generated from our previous algorithm [25], [26], the new 1-km AOD retrievals are improved by 6% and 12% in terms of the fraction of retrievals falling within the EE envelope and MAE, respectively, at urban sites. Moreover, the MAE and RMSE values are reduced by 7% and 5%, respectively, at vegetated sites. On a regional scale, 5% more of AOD retrievals from our algorithm fall within the EE envelope, and MAE and RMSE values also decrease by 18% and 9%, respectively. Moreover, overestimated AOD retrievals from our algorithm are also reduced by 5%. These results suggest that the overall accuracy of AOD retrievals from our new developed algorithm has been improved after considering the influence of the BRDF.

D. Spatial Distributions of Aerosols Over Eastern China

This section performs the comparisons of the spatial coverages, distributions, and variations in aerosol loading among different MODIS AOD products over Eastern China. Fig. 6 shows the two cases considered here: a low-aerosol-load scene on July 14, 2014 [Fig. 6(i)] and a high-aerosol-load scene on August 9, 2014 [Fig. 6(ii)]. All spatial distributions are similar, showing high aerosol loading in the central urban areas and low aerosol loading in the northern and surrounding vegetated areas. Note that different algorithms have different spatial coverages, which is closely related to the applicability of algorithms' particular cloud mask and aerosol schemes. MOD04 3- and 10-km DT products have similar spatial patterns, but they show a large number of missing values, especially in urban areas due to the limitations of the DT algorithm [Fig. 6(i-b) and (i-c) and (ii-b) and (ii-c)]. However, due to its higher spatial resolution, the MOD04 3-km DT product can provide more detailed aerosol information but with a lower spatial continuity. The DB algorithm can retrieve AODs over bright urban areas and provides better spatial continuity than the DT algorithm [Fig. 6(i-d) and (ii-d)]. The spatial coverage of the MOD04 10-km DTB product [Fig. 6(i-e) and (ii-e)] is not as wide because it is based
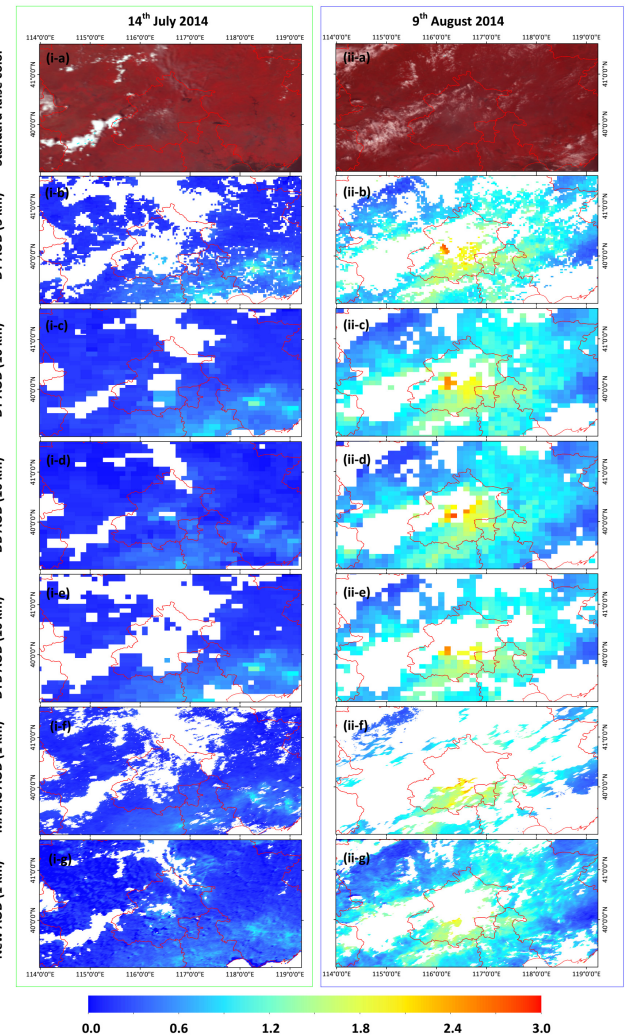

Fig. 6. (a) Standard false color images (channels: 2:4:3), and spatial distributions of (b) MOD04 C6.1 DT (3 km), (c) DT (10 km), (d) DB (10 km), (e) DTB (10 km), (f) MAIAC (1 km), and (g) our new (1 km) AOD data sets for (i) a low-aerosol event on July 14, 2014 and (ii) a high-aerosol event on August 9, 2014 over Eastern China.

on a combination of the highest-quality DT (QA = 3) and DB (QA ≥ 2) AOD retrievals [16]. The MAIAC algorithm allows for aerosol retrievals over the whole surface at a 1-km resolution and can produce more detailed aerosol distributions [Fig. 6(i-f) and (ii-f)]. However, the spatial coverage is overall lower than that of MOD04 products, mainly because of differences in the cloud detection algorithms. Our newly developed algorithm can retrieve AODs over the darkest to brightest surfaces as can both the DB and MAIAC algorithms [Fig. 6(i-g) and (ii-g)]. It can also provide more detailed AOD spatial distributions at a 1-km resolution than can the algorithms generating MOD04 routine AOD products at coarser 3- and 10-km resolutions. Moreover, a wider spatial coverage than the MAIAC AOD product is also seen probably due to a more accurate cloud mask. However, the differences between these two cloud masks need further investigation. Nevertheless, these results illustrate that the newly developed algorithm can better describe the spatial distribution of aerosols at small- to medium-spatial scales.

VI. CONCLUSION

In this paper, a regionally robust aerosol retrieval algorithm at a 1-km resolution is developed for MODIS images of Eastern China. The main challenges faced in aerosol retrievals, i.e., surface reflectance estimation, aerosol-type assumption, and identification of cloud, snow, ice, and water, are dealt with effectively. The RossThick-LiSparse model is used to correct the surface reflectance for BRDF effects. Aerosol types are determined based on time-series analyses of aerosol optical properties derived at local AERONET sites. The UDTCDA, vegetation indices, and brightness temperatures are used to identify and mask all unsuitable pixels. Moreover, gas absorption (especially for H_2O and O_3) is corrected using improved modeled approximations. The aerosol retrieval is performed using the LUT approach on data from Eastern China for the period 2010–2014. The retrievals are validated against the AERONET Version 3 Level 2.0 AOD measurements and compared with current MODIS C6.1 3 and 10 km, and MAIAC 1-km aerosol products.

Results show that our 1-km AOD retrievals agree well with AERONET AOD measurements ($R = 0.929$). Approximately 79% of our retrievals fall within the EE envelope with average MAE and RMSE values of 0.074 and 0.125, respectively, on a regional scale. In addition, the new 1-km AOD retrievals are more accurate than the MOD04 3- and 10-km DT and 10-km DTB AODs. The new algorithm can also significantly reduce overestimations of AOD at urban sites. Moreover, our retrieval algorithm performs slightly better than the DB algorithm on a regional scale. The MAIAC algorithm and our new algorithm perform similarly well and have almost the same metrics at each site and on a regional scale.

Aerosol retrievals over from dark to bright surfaces at a high resolution of 1 km are possible with this newly developed algorithm. The algorithm can provide more detailed and consistent aerosol distributions than operational MOD04 products at coarser resolutions. Moreover, the algorithm can provide a wider spatial coverage than can the MAIAC algorithm. These results illustrate that the new algorithm is robust and can provide more accurate and continuous aerosol information at small- to medium-spatial scales. In the future work, we will focus on obtaining more accurate estimates of surface reflectance and on refining aerosol types in an attempt to expand the application of the algorithm to larger spatial scales.

ACKNOWLEDGMENT

REFERENCES

[1] C. A. Pope, III, *et al.*, "Lung cancer, cardiopulmonary mortality, and long-term exposure to fine particulate air pollution," *J. Amer. Med. Assoc.*, vol. 287, no. 9, pp. 1132–1141, 2002.

[2] L. He, L. Wang, A. Lin, M. Zhang, M. Bilal, and M. Tao, "Aerosol optical properties and associated direct radiative forcing over the Yangtze River Basin during 2001–2015," *Remote Sens.*, vol. 9, no. 746, p. 2017.

[3] W. Qin *et al.*, "Characteristic and driving factors of aerosol optical depth over mainland China during 1980–2017," *Remote Sens.*, vol. 10, no. 7, p. 1064, 2018.

[4] W. Qin, L. Wang, A. Lin, M. Zhang, and M. Bilal, "Improving the estimation of daily aerosol optical depth and aerosol radiative effect using an optimized artificial neural network," *Remote Sens.*, vol. 10, no. 7, p. 1022, 2018.

[5] G. R. Carmichael *et al.*, "Asian aerosols: Current and year 2030 distributions and implications to human health and regional climate change," *Environ. Sci. Technol.*, vol. 43, no. 15, pp. 5811–5817, 2009.

[6] V. Ramanathan and G. Carmichael, "Global and regional climate changes due to black carbon," *Nature Geosci.*, vol. 36, no. 1, pp. 335–358, 2017.

[7] Y. Wang, K.-H. Lee, Y. Lin, M. Levy, and R. Zhang, "Distinct effects of anthropogenic aerosols on tropical cyclones," *Nature Climate Change*, vol. 4, no. 5, pp. 368–373, 2014.

[8] T. A. Jones and S. A. Christopher, "Statistical properties of aerosol-cloud-precipitation interactions in South America," *Atmos. Chem. Phys.*, vol. 10, no. 5, pp. 2287–2305, 2010.

[9] Z. Li, F. Niu, J. Fan, Y. Liu, D. Rosenfeld, and Y. Ding, "Long-term impacts of aerosols on the vertical development of clouds and precipitation," *Nature Geosci.*, vol. 4, no. 12, pp. 888–894, doi: 10.1038/ngeo1313.2011.

[10] J. D. Small, J. H. Jiang, H. Su, and C. Zhai, "Relationship between aerosol and cloud fraction over Australia," *Geophys. Res. Lett.*, vol. 38, no. 23, p. 379, 2011.

[11] A. D. Clarke *et al.*, "Dust and pollution transport on global scales: Aerosol measurements and model predictions," *J. Geophys. Res.*, vol. 106, pp. 32555–32569, Dec. 2001.

[12] Y. J. Kaufman, D. Tanré, L. A. Remer, E. F. Vermote, A. Chu, and B. N. Holben, "Operational remote sensing of tropospheric aerosol over land from EOS Moderate Resolution Imaging Spectroradiometer," *J. Geophys. Res.*, vol. 102, no. D14, pp. 17051–17067, 1997.

[13] Z. Li *et al.*, "Uncertainties in satellite remote sensing of aerosols and impact on monitoring its long-term trend: A review and perspective," *Annales Geophys.*, vol. 27, pp. 2755–2770, Jul. 2009.

[14] Y. J. Kaufman *et al.*, "The MODIS 2.1-μm channel-correlation with visible reflectance for use in remote sensing of aerosol," *IEEE Trans. Geosci. Remote Sens.*, vol. 35, no. 5, pp. 1286–1298, Sep. 1997.

[15] R. C. Levy, L. A. Remer, S. Mattoo, E. F. Vermote, and Y. J. Kaufman, "Second-generation operational algorithm: Retrieval of aerosol properties over land from inversion of Moderate Resolution Imaging Spectroradiometer spectral reflectance," *J. Geophys. Res.*, vol. 112, no. 13, pp. 1–21, 2007.

[16] R. C. Levy *et al.*, "The collection 6 MODIS aerosol products over land and ocean," *Atmos. Meas. Tech.*, vol. 6, no. 11, pp. 2989–3034, 2013, doi: 10.5194/amt-6-2989-2013.

[17] N. C. Hsu, S.-C. Tsay, M. D. King, and J. R. Herman, "Aerosol properties over bright-reflecting source regions," *IEEE Trans. Geosci. Remote Sens.*, vol. 42, pp. 557–569, Mar. 2004.

[18] N. C. Hsu, S. C. Tsay, M. D. King, and J. R. Herman, "Deep blue retrievals of asian aerosol properties during ACE-Asia," *IEEE Trans. Geosci. Remote Sens.*, vol. 44, no. 11, pp. 3180–3195, Nov. 2006.

[19] N. C. Hsu *et al.*, "Enhanced Deep Blue aerosol retrieval algorithm: The second generation," *J. Geophys. Res., Atmos.*, vol. 118, no. 16, pp. 9296–9315, 2013, doi: 10.1002/jgrd.50712.

[20] J. Wei, L. Sun, B. Huang, M. Bilal, Z. Zhang, and L. Wang, "Verification, improvement and application of aerosol optical depths in China Part 1: Inter-comparison of NPP-VIIRS and Aqua-MODIS," *Atmos. Environ.*, vol. 175, pp. 221–233, Feb. 2018.

[21] L. He, L. Wang, A. Lin, M. Zhang, M. Bilal, and J. Wei, "Performance of the NPP-VIIRS and Aqua-MODIS aerosol optical depth products over the Yangtze river basin," *Remote Sens.*, vol. 10, no. 1, p. 117, 2018.

[22] M. S. Wong, K.-H. Lee, J. E. Nichol, and Z. Li, "Retrieval of aerosol optical thickness using MODIS 500×500 m^2, a Study in Hong Kong and the Pearl River Delta Region," *IEEE Trans. Geosci. Remote Sens.*, vol. 48, no. 8, pp. 3318–3327, Aug. 2010.

[23] A. Lyapustin *et al.*, "Multiangle implementation of atmospheric correction (MAIAC): 2. Aerosol algorithm," *J. Geophys. Res. Atmos.*, vol. 116, no. D03211, pp. 1–15, 2011.

[24] M. Bilal, J. E. Nichol, M. P. Bleiweiss, and D. Dubois, "A simplified high resolution MODIS Aerosol Retrieval Algorithm (SARA) for use over mixed surfaces," *Remote Sens. Environ.*, vol. 136, pp. 135–145, Sep. 2013.

[25] J. Wei and L. Sun, "Comparison and evaluation of different MODIS aerosol optical depth products over the Beijing-Tianjin-Hebei region in China," *IEEE J. Sel. Topics Appl. Earth Observ. Remote Sens.*, vol. 10, no. 3, pp. 835–844, Mar. 2017.

[26] J. Wei *et al.*, "An improved high-spatial-resolution aerosol retrieval algorithm for MODIS images over land," *J. Geophys. Res., Atmos.*, vol. 123, no. 21, pp. 12291–12307, 2018.

[27] L. Sun *et al.*, "A universal dynamic threshold cloud detection algorithm (UDTCDA) supported by a prior surface reflectance database," *J. Geophys. Res., Atmos.*, vol. 121, no. 12, pp. 7172–7196, 2016.

[28] A. Smirnov, B. N. Holben, T. F. Eck, O. Dubovik, and I. Slutsker, "Cloud-screening and quality control algorithms for the AERONET database," *Remote Sens. Environ.*, vol. 73, no. 3, pp. 337–349, doi: 10.1016/S0034-4257(00)00109-7.2000.

[29] J. Wei, B. Huang, L. Sun, Z. Zhang, L. Wang, and M. Bilal, "A simple and universal aerosol retrieval algorithm for Landsat series images over complex surfaces," *J. Geophys. Res. Atmos.*, vol. 122, no. 24, pp. 13338–13355, 2017.

[30] J. Wei, Z. Li, Y. Peng, and L. Sun, "MODIS Collection 6.1 aerosol optical depth products over land and ocean: Validation and comparison," *Atmos. Environ.*, vol. 201, pp. 428–440, Mar. 2019. doi: 10.1016/j.atmosenv.2018.12.004.

[31] A. Lyapustin, Y. Wang, S. Korkin, and D. Huang, "MODIS collection 6 MAIAC algorithm," *Atmos. Meas. Techn.*, vol. 11, no. 10, pp. 5741–5765, 2018.

[32] S. Y. Kotchenova and E. F. Vermote, "Validation of a vector version of the 6S radiative transfer code for atmospheric correction of satellite data. Part II. Homogeneous Lambertian and anisotropic surfaces," *Appl. Opt.*, vol. 46, no. 20, pp. 4455–4464, 2007.

[33] S. Y. Kotchenova, E. F. Vermote, R. Matarrese, and F. J. Klemm, "Validation of a vector version of the 6S radiative transfer code for atmospheric correction of satellite data. Part I: Path radiance," *Appl. Opt.*, vol. 45, no. 26, pp. 6762–6774, 2006.

[34] B. A. Bodhaine, N. B. Wood, E. G. Dutton, and J. R. Slusser, "On Rayleigh optical depth calculations," *J. Atmos. Ocean. Technol.*, vol. 16, no. 11, pp. 1854–1861, 1999.

[35] F. Patadia, R. C. Levy, and S. Mattoo, "Correcting for trace gas absorption when retrieving aerosol optical depth from satellite observations of reflected shortwave radiation," *Atmos. Meas. Techn.*, vol. 11, no. 6, pp. 3205–3219, 2018.

[36] C. Gueymard *et al.*, *SMARTS2: A Simple Model of the Atmospheric Radiative Transfer of Sunshine: Algorithms and Performance Assessment*. Cocoa, FL, USA: Florida Solar Energy Center, 1995, pp. 1–78.

[37] D. P. Dee *et al.*, "The ERA-Interim reanalysis: Configuration and performance of the data assimilation system," *Quart. J. Roy. Meteorol. Soc.*, vol. 137, pp. 553–597, Apr. 2011.

[38] X. Yan *et al.*, "A minimum albedo aerosol retrieval method for the new-generation geostationary Meteorological Satellite Himawari-8," *Atmos. Res.*, vol. 207, pp. 14–27, Jul. 2018.

[39] L. Sun *et al.*, "Aerosol optical depth retrieval over bright areas using Landsat 8 OLI images," *Remote Sens.*, vol. 8, no. 1, p. 23, 2016.

[40] W. Wanner, X. Li, and A. H. Strahler, "On the derivation of kernels for kernel-driven models of bidirectional reflectance," *J. Geophys. Res. Atmos.*, vol. 100, no. D10, pp. 21077–21089, 1995.

[41] J. L. Roujean, M. Leroy, and P. Y. Deschamps, "A bidirectional reflectance model of the Earth's surface for the correction of remote sensing data," *J. Geophys. Res. Atmos.*, vol. 97, no. D18, pp. 20455–20468, 1992.

[42] W. Lucht, C. B. Schaaf, and A. H. Strahler, "An algorithm for the retrieval of albedo from space using semiempirical BRDF models," *IEEE Trans. Geosci. Remote Sens.*, vol. 38, no. 2, pp. 977–998, Mar. 2002.

[43] X. Li and A. H. Strahler, "Geometric-optical bidirectional reflectance modeling of the discrete crown vegetation canopy: Effect of crown shape and mutual shadowing," *IEEE Trans. Geosci. Remote Sens.*, vol. 30, no. 2, pp. 276–292, Mar. 1992.
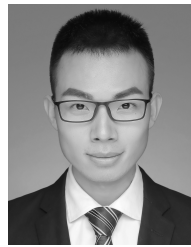
Jing Wei (S'16) received the B.Ec. and M.Ec. degrees in remote sensing science and technology, and photogrammetry and remote sensing from the Shandong University of Science and Technology, Qingdao, China, in 2014 and 2017, respectively. He is currently pursuing the Ph.D. degree in global environmental change with Beijing Normal University.

He has been a Research Assistant with the Chinese University of Hong Kong, Hong Kong, and Tsinghua University, Beijing. His research interests include aerosol and cloud remote sensing and aerosol–cloud-radiation interactions.

Mr. Wei is an AGU Student Member.

Zhanqing Li received the B.Sc. and M.Sc. degrees from the Nanjing University of Information Science and Technology, Nanjing, China, in 1983 and 1989, respectively, and the Ph.D. degree from McGill University, Montreal, QC, Canada, in 1991.

He is currently a Professor with the University of Maryland, College Park, MD, USA. He has authored over 280 papers. His research interests include remote sensing, atmospheric physics, climate and environment focusing on aerosol, cloud, radiation budget, and precipitation.

Dr. Li is a fellow of AMS, AGU, and AAAS. He received numerous awards in United States, Canada, and Germany. He is an Editor of the *Journal of Geophysical Research—Atmospheres*, and a Guest Editor of the *Atmospheric Chemistry and Physics*.

Yiran Peng received the B.Sc. degree in atmospheric science from Peking University, Beijing, China, in 1999, and the Ph.D. degree in atmospheric science from Dalhousie University, Halifax, NS, Canada, in 2005.

She is currently an Associate Professor with the Department of Earth System Science, Tsinghua University, Beijing. Her research interests include aerosol and cloud simulations in global climate models, and aerosol effects on radiation and climate.

Lin Sun received the M.Sc. degree in meteorology from the Nanjing University of Information Science and Technology, Nanjing, China, in 2003, and the Ph.D. degree in cartography and geographic information system from the Institute of Remote Sensing and Digital Earth, Chinese Academy of Science, Beijing, China, in 2006.

He is currently a Professor with the College of Geomatics, Shandong University of Science and Technology, Qingdao, China. His research interests include cloud detection and aerosol optical depth retrieval from satellite data.
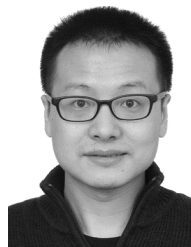
Xing Yan received the B.Sc. degree from Capital Normal University, Beijing, China, and the M.Sc. and Ph.D. degrees from Hong Kong Polytechnic University, Hong Kong, China, in 2011 and 2017, respectively.

He is currently with the College of Global Change and Earth System Science, Beijing Normal University, Beijing, and appointed as a Master Supervisor in 2018. His research interests include aerosol optical depth retrieval, satellite-based anthropogenic aerosol, and atmospheric environment pollution.